Atom Indonesia

Journal homepage: http://atomindonesia.brin.go.id

Monte Carlo Simulation of Pediatric Chest Radiography: Validation of the Irradose Through Comparison with MCNP

O. El Basraoui[1], O. Qassimi[1], O. Kabach[3], M. Y. Messous[2], N. Tahiri[1], F. Arianto[4], O. El Bounagui[1*]

[1] *LaMCScI, Faculty of Sciences, Mohammed V University in Rabat, Morocco*
[2] *Material Sciences Unit (USM/DERS), National Center for Energy, Sciences and Nuclear Techniques (CNESTEN), Rabat, Morocco*
[3] *LPMS, faculty of sciences, Ibn Tofail University, Kenitra, Morocco*
[4] *Department of Physics, Faculty of Science and Mathematics, Diponegoro University, Semarang 50275, Indonesia*

ARTICLE INFO

Article history:
Received 29 July 2025
Received in revised form 26 October 2025
Accepted 17 November 2025

Keywords:

Absorbed dose
Monte Carlo simulation
MCNP code
Biological tissues
HCNO
Cylindrical phantom

ABSTRACT

Radiological examinations are essential for medical diagnostics, but accurate estimation of dose deposition is crucial for patient safety, particularly in pediatric patients. This study employs Monte Carlo simulations with the MCNP code and a newly developed custom program, Irradose, to analyze photon dose deposition in a cylindrical phantom representing the thorax of a 10-year-old child. Two tissue-equivalent compositions were modeled: water and a more realistic HCNO-based soft tissue mixture. Depth-dose distributions obtained with Irradose were compared to MCNP results. Both codes predicted a maximum dose at 2 cm depth, followed by exponential fall-off, with deviations remaining below 5% across the depth range. These results validate Irradose as a reliable and computationally efficient tool for pediatric chest dosimetry in phantom studies. While limited to simplified geometries, this work demonstrates the potential of Irradose for use in preliminary dose assessments and as a complement to established Monte Carlo codes.

INTRODUCTION

Radiological examinations such as X-ray imaging and Computed Tomography (CT) are indispensable in medical diagnostics, enabling the detection and monitoring of various diseases [1]. However, these procedures expose patients to ionizing radiation, making accurate dose estimation essential for radiation protection and optimization [2]. This concern is especially critical in pediatric imaging, where patients exhibit higher tissue radiosensitivity and longer life expectancy than adults. Studies have shown that children may receive effective doses up to three times higher than adults for equivalent diagnostic information [3,4], with typical pediatric chest X-ray doses ranging from 0.02 to 0.2 mGy per exposure [5].

Given these increased risks, optimizing pediatric radiological procedures requires reliable dosimetric tools capable of estimating absorbed doses with high precision [6]. Monte Carlo simulation methods are considered the gold standard for radiation transport modeling, providing detailed information on energy deposition within heterogeneous materials [7-11]. Among these, the MCNP code is widely used in medical physics and radiation protection due to its accuracy and versatility [12]. Nevertheless, MCNP simulations can be computationally intensive and time-consuming, particularly when modeling complex geometries or performing large numbers of particle histories [13].

To address these challenges, this study presents the development and validation of a custom Monte Carlo simulation program, Irradose, specifically optimized for low-energy photon dosimetry in diagnostic radiology. Unlike general-purpose codes such as MCNP [8,13], Irradose is lightweight, faster to execute, and tailored to simulate key photon interactions (photoelectric and Compton) relevant to the diagnostic range

*Corresponding author.
E-mail address: elbounagui@gmail.com
DOI: https://doi.org/10.55981/aij.2026.1763

(60-150 keV) [14]. Its simplified structure significantly reduces computational time and resource demand, making it particularly advantageous for pediatric dosimetry studies and for use in resource-limited or educational environments [15].

The objective of this work is to validate Irradose by comparing its dose calculation results with those obtained using MCNP in a simplified pediatric chest phantom. The comparison focuses on depth-dose distributions for two tissue-equivalent materials, water and HCNO soft tissue composition, to evaluate both the accuracy and computational performance of Irradose. By validating this custom code, the study contributes to the broader effort of developing accessible, reliable dosimetric tools for pediatric radiology [16].

METHODS

Photon interaction in matter

The type of interaction that a photon undergoes is determined by its cross-section, which depends on its energy and the medium. Figure 1 shows the cross-section for various interactions in water. At a typical radiology exam, X-ray energies (60-150 keV), the cross-section for pair production (k) is zero, as there is a lower energy threshold of 1.022 MeV for this interaction [17]. Therefore, for the radiology exam, X-rays, it is only necessary to consider the photoelectric (τ) and Compton (σ) cross-section [18].

In the photoelectric effect, an incoming photon transfers all of its energy to a tightly bound electron when it interacts with matter. The photoelectron is then ejected from the atom at an angle of θ with the kinetic energy T.

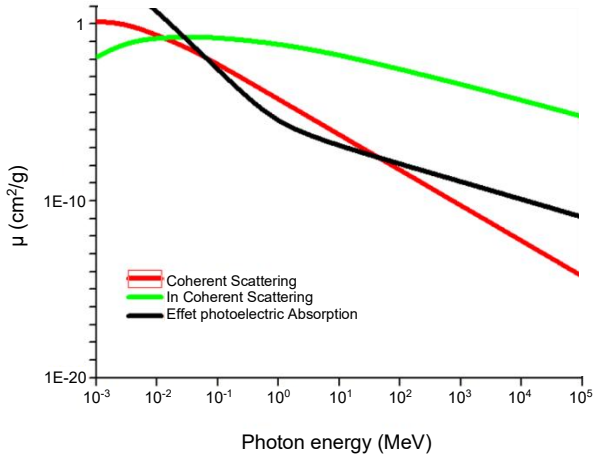

Fig. 1. Photon interaction cross-sections in water as a function of energy.

In this case, the incident photon interacts with an essentially unbound electron in another shell. Following this interaction, the electron is ejected with kinetic energy T, while the photon is scattered at an angle θ with new energy E_1 following Eq. (1) [19,20].

$$E_1 = \frac{E_0}{1+\alpha(1-cos\theta)} \quad (1)$$

Where E_0 is the energy of the incident photon.

Where $\alpha = \frac{E_0}{m_0 c^2}$ is the constant.

Monte Carlo simulations have been extensively used in the study of medical imaging for dose calculations, particularly in soft tissues. For instance, Monte Carlo calculations have been performed to estimate the dose to the breast during mammography, revealing the predominance of photoelectric absorption at low X-ray energies [21].

Path length sampling

There are two basic sampling techniques required to model photon transport and penetrate through matter. The first of these is path length sampling, which determines how far the photon will travel before undergoing an interaction. If the distance to the interaction is greater than the dimension of the target, then the photon will not interact within the tissue and will not contribute to the dose. Conversely, if the distance to the interaction is less than the dimension of the target, the photon will interact, and therefore the photon transport must be modelled.

In order to sample the path length of an incident photon, we assume that the photon undergoes simple exponential attenuation prior to interaction. The probability of interaction is then given by Eq. (2), where x is the distance travelled before interaction occurs and μ is the total linear attenuation coefficient, which is equal to the sum of the photoelectric and Compton interaction coefficients [21].

$$P(x) = 1 - \exp(-\mu x) \quad (2)$$

We may sample the path length x, Eq. (3), where ξ is a uniform random number between 0 and 1, and x is then compared to the dimension of the target and is used the determine whether or not the photon interacts.

$$x = \frac{1}{\mu} ln\left(\frac{1}{\xi}\right) \quad (3)$$

Atom interaction

In the first step, we determine the total attenuation coefficient of the chemical composition target material (HCNO) using the following formula in Eq. (4):

$$\mu_{Target}(E) = \sum \mu_{atom}(E) \quad (4)$$

where μ_{Target} and μ_{atom} are the total attenuation coefficient for the target and the attenuation coefficient for each atom in the target, respectively.

We can deduce the probability of a photon interacting with a particular atom by calculating the X-ray attenuation coefficient of the target and the attenuation coefficients of each atom in the material.

Indeed, if the random number ξ is located:

If $\xi \leq \frac{\mu_{\mathrm{H}}(\mathrm{E})}{\mu_{\mathrm{Target}}(\mathrm{E})}$ the photon interacts with a hydrogen atom, H.

If $\xi \leq \frac{\mu_{\mathrm{H}}(\mathrm{E})+\mu_{\mathrm{C}}(\mathrm{E})}{\mu_{\mathrm{Target}(\mathrm{E})}}$ the photon interacts with the carbon atom, C.

If $\xi \leq \frac{\mu_{\mathrm{H}}(\mathrm{E})+\mu_{\mathrm{C}}(\mathrm{E})+\mu_{\mathrm{N}}(\mathrm{E})}{\mu_{\mathrm{Target}}(\mathrm{E})}$ the photon interacts with the nitrogen atom, N.

If $\xi \leq \frac{\mu_{\mathrm{H}}(\mathrm{E})+\mu_{\mathrm{C}}(\mathrm{E})+\mu_{\mathrm{N}}(\mathrm{E})+\mu_{\mathrm{O}}(\mathrm{E})}{\mu_{\mathrm{Target}}(\mathrm{E})}$ the photon interacts with the oxygen atom, O.

After having selected the interaction atom, the same procedure is used to determine the type of interaction.

Figure 2 presents the summary of X-ray interactions. (a) Primary, unattenuated incident beam does not interact with the material, (b) Photoelectric absorption results in the total removal of the incident X-ray photon with energy greater than the binding energy of the electron in its shell, with excess energy distributed to the kinetic energy of the photoelectron, (c) Rayleigh scattering is an interaction with an electron (or whole atom) in which no energy is exchanged, and incident X-ray energy equals scattered X-ray energy with a small angular change in direction, (d) Compton scattering interactions occur with essentially unbound electrons, with transfer of energy shared between the recoil electron and the scattered photon, with energy exchange described by the Klein–Nishina formula.

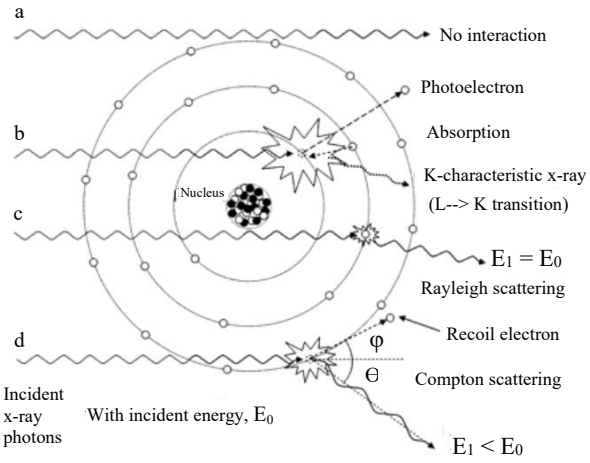

Fig. 2. Illustrative summary of X-ray interactions.

Interaction type sampling

If the path length sampling reveals that the photon does interact in the target, the type of interaction must then be determined using interaction sampling. This is done by first computing the relative probabilities of each type of interaction. Equation 6 shows the probability of the photoelectric effect apparition, where τ is the photoelectric cross-section and σ is the Compton cross-section, Eq. (5).

$$\sigma = \sigma_{coh} + \sigma_{inc} \quad (5)$$

$$P_{\tau} = \frac{\tau}{\tau+\sigma} \quad (6)$$

A similar equation for the Compton coherent interaction is found by replacing the τ in the numerator with σ_{coh}. We can sample the interaction type by generating a uniform random number ξ, between 0 and 1 and defining that:

If $\xi \leq p_{\tau}$ then the interaction is photoelectric.

If $p_{\tau} \leq \xi \leq p_{\mathrm{coh}}$ then the interaction is coherent Compton.

If $p_{\tau} \leq \xi \leq p_{\mathrm{inc}}$ then the interaction is incoherent, Compton.

Photoelectric interaction

If the interaction is photoelectric, the simulation is straightforward. As discussed in an earlier subsection, the incident photon transfers all its energy to liberate the photoelectron with a kinetic energy T. The electron binding energies for the K-shell and L-shell depend on the atomic

number [22]. When modelling biological tissue using the HCNO composition, the transport of the resulting photoelectron can be simplified by considering the maximum range of the electron in the tissue. Since the highest energy of the X-rays under consideration is 150 keV, the most energetic photoelectrons possible will have an energy of 150 keV. At this energy, the range of electrons in biological tissue is 0.0269 cm, as given by the formula of Katz and Penfold in Eq. (7) [23].

$$R_{\left(g/cm^2\right)} = 0.412\ T^{1.256-0.0954\ \ln(T)} \quad (7)$$

We may also consider that the photoelectron's kinetic energy can be obtained using the equation $T = E_0$. A typical thickness of a thorax target used in radiological simulation is 20 cm; therefore, the electron's range is clearly much less than the dimensions of the phantom. For this reason, we can assume that the electron deposits all its energy in the target.

Incoherent compton and coherent interaction

This type of interaction is obtained when the random number drawn is greater than the probability of the occurrence of the photoelectric effect. Since the relative amount of energy transferred to the scattered photon and the electron will depend on the scattering angle, the event must generate such that it follows the expected angular distribution given by Eq. (8), where r_0 is the classical electron radius and has a value of 2.8179 x 10^{-13} cm.

$$g(\theta)d\theta d\varphi = \frac{r_0^2}{2}\left[\left(\frac{E'}{E_0}\right)^3 + \frac{E'}{E_0} - \left(\frac{E'}{E_0}\right)^2 sin^2(\theta)\right] sin(\theta)\, d\theta d\varphi \quad (8)$$

This can be accomplished by first approximating the function in Eq. (8) by the expression in Eq. (9).

$$f(\theta)d\theta d\varphi = \frac{r_0^2}{2}\left(\frac{E'}{E_0}\right) sin(\theta)\, d\theta d\varphi \quad (9)$$

We may then generate a random number u using Eq. (9), where ξ is a uniform random number between 0 and 1. The scattering angle of photon is given by Eq. (10).

$$\theta = \cos^{-1}(1 - u) \quad (10)$$

where u is obtained by the Eq. (11) as follow:

$$u = \left(\frac{1}{\xi} - 1\right)\frac{1}{\alpha} \quad (11)$$

Then the scattering angle θ follows the distribution given by Eq. (8).

The decision whether to accept the value of is based on a weight factor given by $w = \frac{g}{f}$. If $w > 2\xi$ we accept θ, otherwise we generate another random number ξ and start the process over. The factor of 2 can be determined iteratively and is equal to the maximum possible value of the number u [18].

Coherent scattering occurs with low-energy X-rays. When they interact with an attenuating medium, the photons do not have enough energy to liberate electrons from their bound states because their energy is well below the electrons' binding energies. Consequently, no energy is transferred, and the only change is a change in the photon's direction (scattering). Coherent scattering is therefore a major interaction process observed in the presence of low X-ray energy.

Geometry and phantom

To accurately simulate the thoracic region of a paediatric patient, a simplified cylindrical phantom was developed. This phantom effectively models the chest of a 10-year-old child, a demographic that is highly susceptible to the effects of ionising radiation due to its elevated radiosensitivity and longer life expectancy [24,25]. The design balances anatomical relevance with computational simplicity, which is crucial for achieving efficient and precise dose estimations using Monte Carlo simulations.

The phantom was modeled as a right circular cylinder with a radius of 15 cm and a height of 20 cm, approximating the average thoracic dimensions of a child in this age group (see Fig. 3). This configuration reflects standard parameters used in previous pediatric dosimetric studies and offers sufficient volume to analyze dose distribution through depth, while minimizing boundary effects [26].

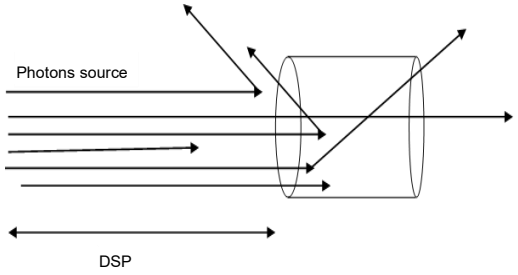

Fig. 3. Phantom geometry.

Initially, the cylindrical phantom was filled with liquid water to serve as a tissue-equivalent material, as recommended in ICRU Report 44, owing to water's similarity in density and atomic composition to soft tissues [27]. In a second step, the phantom composition was refined using a realistic soft tissue mixture composed of hydrogen (H), carbon (C), nitrogen (N), and oxygen (O), referred to as the HCNO composition, based on reference data from the same report. This adjustment allowed for better modeling of the heterogeneity of human tissues and the interaction of photons with elements more representative of biological materials [27].

The X-ray source was placed at a Source-to-Skin Distance (SSD) of 80 cm, oriented perpendicular to the anterior surface of the cylinder. This setup reproduces a Posterior-Anterior (PA) thoracic examination, commonly used in pediatric chest radiography [28]. The photon beam was modeled as a monoenergetic source at 150 keV, typical of pediatric radiological imaging [29], with uniform angular distribution over the cylindrical surface to simulate clinical exposure conditions.

By combining this geometric configuration with accurate material definitions, the simulation setup enables a reliable assessment of depth-dose distributions and the impact of tissue composition on photon energy deposition, supporting the overall goal of improving pediatric radiation protection.

Irradiation dose calculations

A custom Monte Carlo simulation program was developed in parallel with MCNP simulations to evaluate photon dose deposition during paediatric radiological examinations. Designed specifically for low-energy photon transport through biological tissue, the code offers a simplified yet efficient alternative to commercial Monte Carlo software. The main objective was to reproduce physical interactions while minimising computational complexity. The simulation considered the two dominant photon interactions in the diagnostic X-ray energy range (60-150 keV): Photoelectric effect, where the entire photon energy is transferred to a bound electron, and the photoelectron deposits its energy locally, assuming its short range in soft tissues; Compton scattering, where the photon is scattered at a specific angle and energy, while a recoil electron is produced. The angular and energy distributions were sampled according to Klein-Nishina differential cross-sections, using rejection sampling techniques [7].

To determine the type of interaction, the code employed probabilistic interaction sampling based on relative cross-sections (photoelectric vs. Compton). Once the photon had deposited all its energy or exited the geometry, the absorbed dose was computed using the total energy deposited in the phantom and its mass [30]. Additionally, the program generated energy spectra, depth-dose distributions, and angular distributions of scattered photons (see Fig. 4). The program works as follows:

As shown in Fig. 5, the phantom geometry used in this study is a cylinder with a radius of R = 10 cm and a height of h = 20 cm. The average dose deposited in the target will be calculated by taking into account the elementary doses deposited by each photon during its travel, as explained by the flowchart in Fig. 3. The program is run using the input file "croshcno.dat", which is drawn from the international library XCOM [15].

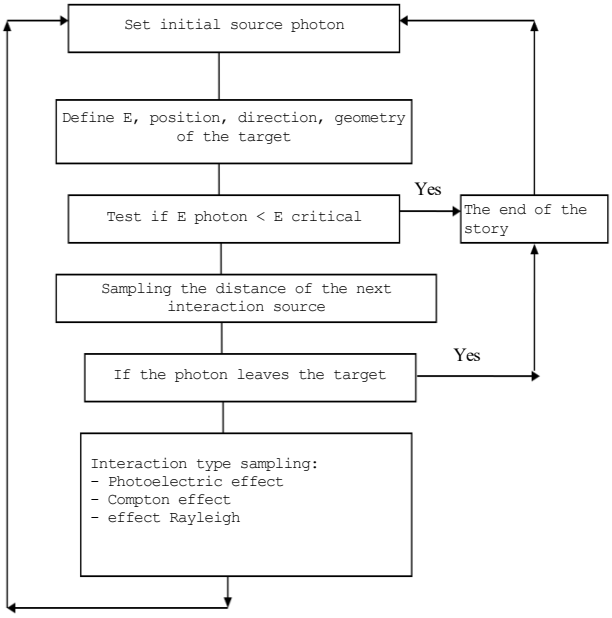

Fig. 4. Irradose flowchart for photon transport and interaction in a target medium.

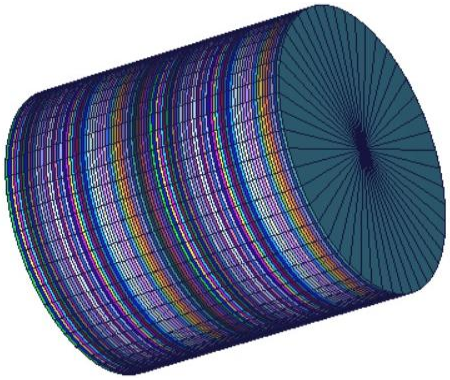

Fig. 5. Discretized cylindrical phantom geometry used for MCNP dose simulation.

For the calculation of the average dose (D) deposited by photon, we use Eq. (12) [5,31].

$$D = \frac{1}{m}\ \frac{1}{N_s}\sum_{j=1}^{N_s}\left(\sum_{i=1}^{N_c}\Delta E^{i,j}\right) \quad (12)$$

Where m is the total mass of the target and N_s is the number of simulations, N_c is the number of collisions between photons and electrons, and $\Delta E^{i,j}$ is the differential energy deposited after each interaction.

Using this program in the case of a thorax of a child simulated by a cylinder of the radiological dose deposited by each photon. To ensure statistical reliability 10^9, photon histories were simulated per run

MCNP simulation configuration

The dosimetric simulations presented in this study were conducted using version 6.2 of the Monte Carlo N-Particle Transport Code (MCNP), which was developed by Los Alamos National Laboratory [12,21,28]. MCNP is a highly versatile, widely validated Monte Carlo code used to simulate the transport of photons, electrons, neutrons, and other particles within complex, three-dimensional geometries. It is particularly prominent in the fields of medical physics, radiation protection, and radiation dosimetry due to its ability to precisely model radiation interactions within heterogeneous media [12].

In this work, photon transport was exclusively modeled by employing the (MODE p) setting, aligning with the diagnostic imaging context of the simulation. This configuration enables the inclusion of key low-energy photon interactions such as photoelectric absorption, Compton scattering, and Rayleigh scattering, which dominate in the diagnostic X-ray energy range [8]. These interactions were modeled using cross-section data from the evaluated photon data library (EPDL97) [30], integrated within MCNP.

To ensure precise energy deposition modeling, especially significant in pediatric radiology, the photon transport cutoff energy was set to 1 keV. This threshold allows the simulation to capture the influence of low-energy scattered photons on absorbed dose distribution with high fidelity [31].

The simulated phantom was discretized into 100 axial layers, each defined as an MCNP cel using flat surfaces at 2 mm intervals from 0 to 20 cm along the x-axis. Each layer was modelled with the properties of soft tissues (ρ=1.0 g/cm³), laterally confined by a cylindrical surface with a radius of 10 cm.

The photon source was defined at position (-80,0,0) and directed along the positive x-axis. A monoenergetic source of 150 keV and an area source of radius 0.1 cm to simulate a finite source spot size, see Fig. 5.

To quantify dose deposition, F6 tallies were assigned to all 100 tissue cells. The F6 tally in MCNP reports the average energy deposition per unit mass (MeV/g), which was converted to gray (Gy) using the conversion factor 1.60218×10^{-16} J/MeV. To ensure statistical reliability, 10^6 photon histories were simulated per run. This number was selected to achieve relative errors under 5% across all tallied regions, maintaining a balance between simulation precision and computational time.

RESULTS AND DISCUSSION

Within the diagnostic range of 60-150 keV, the dominant interactions of photons with soft tissue are photoelectric absorption and Compton scattering. Pair production has a threshold energy of 1.022 MeV and therefore does not occur within this range. This selection is consistent with ICRU Report 44 and EPDL97 cross-section data [14,30]. Although Rayleigh scattering was considered negligible for energy deposition, it is included in MCNP validation for completeness.

Figures 6 and 7 illustrate the normalized dose distribution as a function of depth in cm for two different materials, soft tissue-equivalent material (HCNO) and water (H2O), respectively. In both cases, the dose distribution was calculated using two Monte Carlo-based simulation tools, MCNP (black curve) and the custom code Irradose (red curve). The aim of these simulations is to evaluate and validate the accuracy of the Irradose code in modelling photon dose deposition, particularly in diagnostic radiology contexts.

Both figures show a typical depth-dose profile for low-energy photon beams a build-up region near the surface, followed by a maximum dose, and a gradual exponential fall-off with increasing depth. This behavior is characteristic of photon interactions in soft biological tissues. The comparison between the MCNP and Irradose reveals a strong agreement in the overall shape and trend of the dose profiles for both materials. The location and amplitude of the maximum dose are consistent across both codes, suggesting that Irradose successfully reproduces the essential physics of photon transport and energy deposition.

The slight difference observed in Fig. 6, starting from a depth of 10 cm, can be attributed to the differences between the X-COM and ENDF cross-section libraries used respectively in the Irradose and MCNP 6.2 codes.

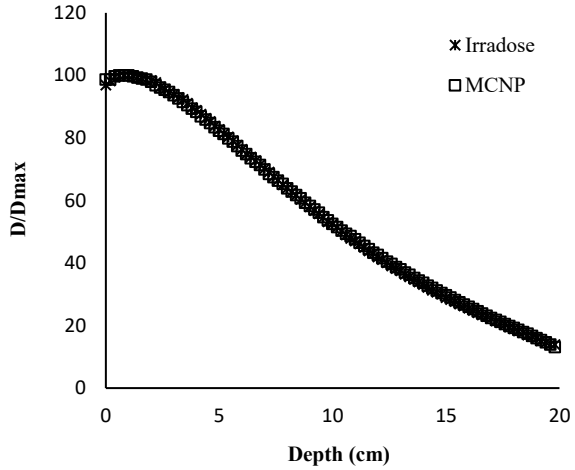

Fig. 6. Comparison of normalized depth-dose distribution (D/Dmax) in soft tissue (HCNO) using MCNP and Irradose codes.

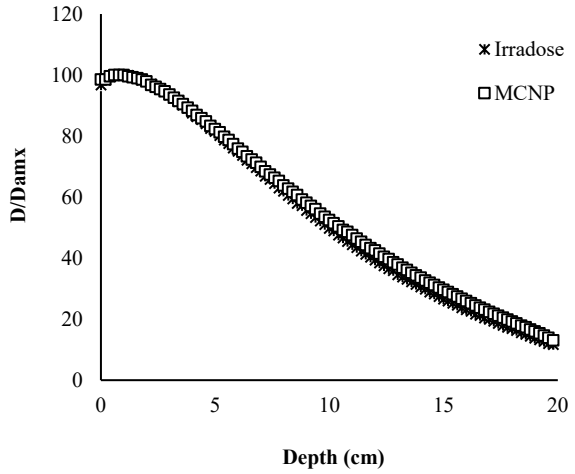

Fig. 7. Comparison of normalized depth-dose distribution (D/Dmax) in water (H2O) using MCNP and Irradose codes.

The minor differences observed between the curves, especially beyond a depth of 10 cm, can be attributed to differences in the cross-section libraries, photon interaction models, and variance reduction techniques used by the two codes.

For the HCNO material (see Fig. 6), which more accurately represents the composition of biological tissue, the match between the two codes remains excellent throughout the depth range. The average deviation between MCNP and Irradose results was below 5% across all depths, reaching approximately 4.6% at 15 cm. The maximum dose was achieved at a depth of about 2 cm for both codes. A similar level of agreement is observed in the water phantom (see Fig. 7), though the dose fall-off with Irradose is slightly slower beyond mid-depth. These small deviations remain within acceptable limits for medical dosimetry applications and do not significantly impact the overall accuracy of dose prediction. The results validate Irradose as a reliable and computationally efficient tool for simulating dose distribution in diagnostic radiology. Its performance closely parallels that of MCNP, a widely recognized benchmark in Monte Carlo radiation transport. Therefore, Irradose can be used with confidence in routine dosimetric assessments, particularly in environments with limited resources where faster simulations may be advantageous.

In order to provide additional insight into this work, we can use the Irradose program to study the energy absorption spectrum of the incident photons and the energy absorption spectrum of the backscattered photons, as illustrated in Figs. 8-11. These graphical representations show the effect of absorbed photons on the dose increase within the target as well as in the nearby organs. It can also be added that in the air surrounding the patient's head, the air atoms could be ionized due to the flux of backscattered photons, which could cause respiratory difficulties for patients during frequent radiological examinations.

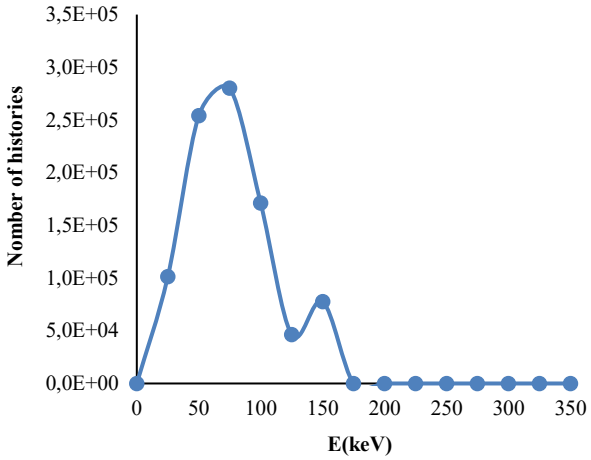

Fig. 8. The energy absorption spectrum for the H_2O phantom.

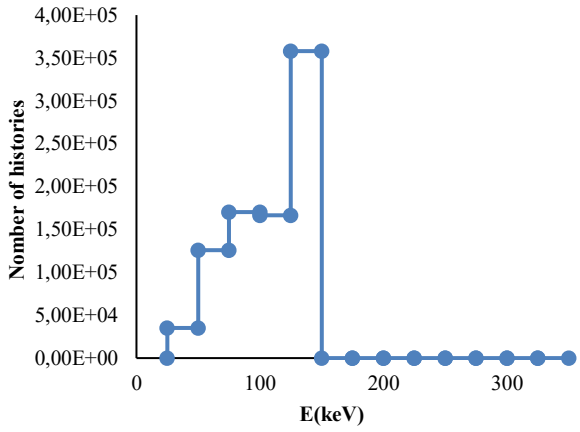

Fig. 9. Energy spectrum of backscattered and leaked photons for H_2O phantom.

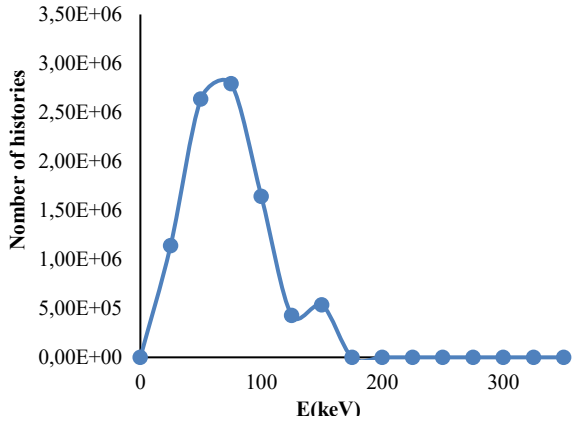

Fig. 10. The energy absorption spectrum for the HCNO phantom.

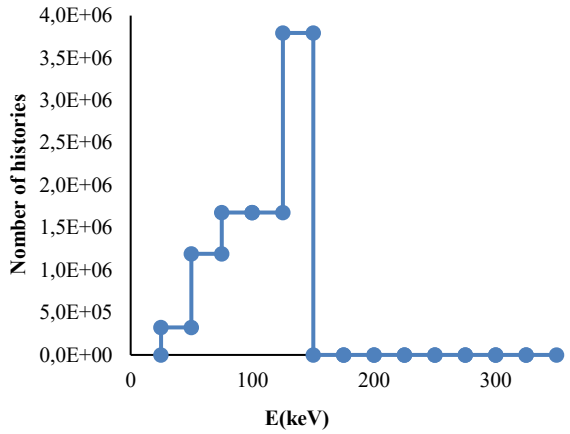

Fig. 11. Energy spectrum of backscattered and leaked photons for HCNO phantom.

CONCLUSION

This work presented the validation of the custom Monte Carlo code Irradose for photon dose estimation in pediatric chest radiography. The comparison with MCNP showed excellent agreement, with deviations below 5% across all depths and a maximum dose occurring at approximately 2 cm in both water and HCNO phantoms. These results confirm that Irradose accurately models photon transport and energy deposition within the diagnostic energy range (60-150 keV).

In addition to depth dose analysis, Irradose was also used to investigate the energy absorption spectra of incident and backscattered photons, providing further insight into photon energy transfer and secondary radiation behavior. The analysis revealed that backscattered photons contribute to low-level energy deposition in surrounding air regions, a finding consistent with photon scattering theory and relevant for evaluating stray radiation exposure during frequent examinations.

Irradose's unique contribution lies in its simplified and transparent implementation of key photon interactions, photoelectric and Compton, allowing researchers and students to model diagnostic photon transport using modest computational resources. While this study was limited to a monoenergetic source and a simplified cylindrical phantom, the validated consistency with MCNP establishes a strong foundation for future extensions.

Future work will focus on integrating polyenergetic X-ray spectra, heterogeneous anatomical models, and two and three-dimensional dose mapping capabilities to enhance clinical realism. These developments aim to make Irradose a practical and educational tool for improving radiation protection and dose optimization in pediatric diagnostic imaging.

ACKNOWLEDGMENT

The authors declare that they have not received any financial or personal assistance from anyone whom we should acknowledge.

AUTHOR CONTRIBUTION

O. El Basraoui, O. Qassimi, and O. El Bounagui equally contributed as the main contributors of this paper. All authors read and approved the final version of the paper.

REFERENCES

1. K. Alzyoud, S. Al-Murshedi, and A. England, Health Phys. **126** (2024) 156.
2. G. K. Korir, J. S. Wambani, I. K. Korir *et al.*, Health Phys. **105** (2013) 522.
3. V. A. Vinnikov and O. Belyakov, Health Phys. **119** (2020) 83.
4. A. Arectout, H. Boukhal, M. Jarmouni *et al.*, Nucl. Anal. **4** (2025) 100141.
5. R. Jannah, R. Munir, and E. R. Putri, Atom Indones. **49** (2023) 145.
6. S. Purnami, S. Nurhayati, M. Syaifudin *et al.*, Atom Indones. **43** (2017) 75.
7. H. Mori, K. Koshida, O. Ishigamori *et al.*, Health Phys. **107** (2014) S202.
8. P. Andreo, Phys. Med. Biol. **36** (1991) 861.
9. J. El Asri, O. El Bounagui, N. Tahiri *et al.*, Atom Indones. **47** (2021) 17.

10. H. Erramli, O. Elbounagui, M. A. Misdaq *et al.,* Nucl. Instrum. Methods Phys. Res., Sect. B. **263** (2007) 127.
11. J. El Asri, O. El Bounagui, N. Tahiri *et al.,* Nucl. Technol.. **205** (2019) 1236.
12. D. B. Pelowitz, MCNPX User's Manual Version 2.5.0, Los Alamos National Laboratory Report LA-CP-05-0369, Los Alamos (2005).
13. J. K. Shultis and A. A. Bahadori, AN MCNP6 PRIMER. Version 1.0, Kansas State University, Department of Mechanical and Nuclear Engineering, Manhattan (2024) 1.
14. International Commission on Radiation Units and Measurements (ICRU), Tissue Substitutes in Radiation Dosimetry and Measurement, (ICRU Report 44), ICRU, Bethesda (1989) 1.
15. J. H. Hubbell, Phys. Med. Biol. **44** (1999) R1.
16. F. A. Mettler, W. Huda, T. T. Yoshizumi *et al.,* Radiol. **248** (2008) 254.
17. D. A. Schauer and O. W. Linton, Radiol. **253** (2009) 293.
18. J. M. Boone, O. Velazquez, and S. R. Cherry, Mol. Imag. **3** (2004) 149.
19. A. S. N. Rao, A. Perumallu, and G. K. Rao, Physica B+C. **124** (1984) 96.
20. Y. Li, T. Su, L. Sheng *et al*., Phys. Lett. B. **868** (2025) 139650.
21. W. Wang, R. Qiu, L. Ren *et al*., Med. Phys. **44** (6) (2017) 2503.
22. M. Y. Amusia, Atomic Photoeffect, Plenum Press, New York (1990) 1.
23. R. Katz and A. S. Penfold, Rev. Mod. Phys. **24** (1952) 28.
24. International Commission on Radiological Protection (ICRP), The 2007 Recommendations of the International Commission on Radiological Protection (ICRP Publication 103), Elsevier, Oxford (2007) 1.
25. D. J. Brenner, C. D. Elliston, E. J. Hall *et al*., Am. J. Roentgenol. Radium Ther. **176** (2001) 289.
26. A. Khursheed, M. C. Hillier, P. C. Shrimpton *et al*., Br. J. Radiol. **75** (2002) 819.
27. P. D. Deak, Y. Smal, and W. A. Kalender, Radiol. **257** (2010) 158.
28. T. Goorley, M. James, T. Booth *et al*, Initial MCNP6 Release Overview – MCNP6 Version 1.0 (LA-UR-13-22934), Los Alamos National Laboratory, Los Alamos (2013) 1.
29. J. T. Bushberg, J. A. Seibert, E. M. Leidholdt Jr *et al.,* The Essential Physics of Medical Imaging (Third Edition), Wolters Kluwer Health/Lippincott Williams & Wilkins (LWW), Philadelphia (2011) 1.
30. D. E. Cullen, M. H. Chen, J. H. Hubbell *et al*., Tables and Graphs of Photon-Interaction Cross Sections from 10 eV to 100 GeV Derived from the LLNL Evaluated Photon Data Library (EPDL), Lawrence Livermore National Laboratory (LLNL), Livermore, CA (1989) VII.
31. K. Boutis, J. Fischer, S. B. Freedman *et al*., J. Emerg. Med. **47** (2014) 36.